Ma *et al. Energy Mater* 2024;4:400059
DOI: 10.20517/energymater.2023.109

Energy Materials

Article

Open Access

Check for updates

Synergetic effect of block and catalysis on polysulfides by functionalized bilayer modification on the separator for lithium-sulfur batteries

Yitian Ma[1], Linqing Chang[1], Dawei Yi[1], Meng Liu[1], Peichun Wang[1], Shuliang Luo[1], Zhiyun Zhang[1], Yan Yuan[2,*], Hai Lu[1,*]

[1]School of Materials Science and Engineering, Xi'an University of Science and Technology, Xi'an 710054, Shaanxi, China.
[2]School of Metallurgical Engineering, Xi'an University of Architecture and Technology, Xi'an 710055, Shaanxi, China.

(Correspondence to: Dr. Hai Lu, School of Materials Science and Engineering, Xi'an University of Science and Technology, No. 58, Yanta Road, Xi'an 710054, Shaanxi, China. E-mail: lhxust@126.com; Dr. Yan Yuan, School of Metallurgical Engineering, Xi'an University of Architecture and Technology, No. 13, Yanta Road, Xi'an 710055, Shaanxi, China. E-mail: lingyi21@126.com

How to cite this article: Ma Y, Chang L, Yi D, Liu M, Wang P, Luo S, Zhang Z, Yuan Y, Lu H. Synergetic effect of block and catalysis on polysulfides by functionalized bilayer modification on the separator for lithium-sulfur batteries. *Energy Mater* 2024;4:400059. https://dx.doi.org/10.20517/energymater.2023.109

Received: 18 Dec 2023 **First Decision:** 20 Mar 2024 **Revised:** 25 Apr 2024 **Accepted:** 8 May 2024 **Published:** 6 Jun 2024

Academic Editors: Wei Tang, Jinqiang Zhang **Copy Editor:** Fangling Lan **Production Editor:** Fangling Lan

Abstract

One crucial problem hindering the commercial application of lithium-sulfur batteries with high theoretical specific energy is the ceaseless shuttle of soluble lithium polysulfides (LiPSs) between cathodes and anodes, which usually leads to rapid capacity fade and serious self-discharge issues. Herein, a unique bilayer coating strategy designed to modify the polypropylene separator was developed in this study, which consisted of a bottom zeolite (SSZ-13) layer serving as a LiPS movement barrier and a top ZnS layer used for accelerating redox processes of LiPSs. Benefiting from the synergetic effect, the bilayer-modified separator offers absolute block capability to LiPS diffusion, moreover, significant catalysis effect on sulfur species conversion, as well as outstanding lithium-ion (Li^+) conductivity, excellent electrolyte wettability, and desirable mechanical properties. Consequently, the assembled lithium-sulfur cell with the SSZ-13/ZnS@polypropylene separator demonstrates excellent cycle stability and rate capability, showcasing a capacity decay rate of only 0.052% per cycle at 1 C over 500 cycles.

Keywords: Lithium-sulfur battery, polysulfide, zeolite, ZnS, separator modification

INTRODUCTION

Lithium-ion batteries (LIBs) have significantly boosted rapid growth of high-performing mobile devices and electric vehicles[1]. However, further increase in energy density remains necessary for the industry requirements. In this case, lithium-sulfur (Li-S) batteries are considered as one of the most attractive energy storage devices on account of a high specific capacity (1,675 mAh g^{-1}) and mass energy density (2,600 Wh kg^{-1})[2,3]. Nevertheless, different from the intercalation mechanism in LIBs, Li-S chemistry undergoes a complex solid-liquid-solid conversion procedure[4,5], generating long-chain lithium polysulfides (LiPSs, Li_2S_n, $4 \leq n \leq 8$) during the cell operation. These soluble LiPSs can migrate to the lithium anode and deposit on its surface as solid Li_2S_2/Li_2S by corrosion reaction, further producing the notorious "shuttle effect"[6]. Meanwhile, accompanied by iterative lithium plating/stripping, lithium dendrites grow on the anode, increasing polarization and even security incidents[7,8].

Massive strategies for settling obstinate problems mentioned above have been proposed such as electrolyte optimization[9], sulfur host design[10] and separator coating[11]. Among them, separators are advantageous platforms to address critical issues such as dendrite proliferation, "shuttle effect", and interfacial instability. At the same time, modifying commercial separators is one of the preferred routes due to its simplicity and effectiveness. Currently, research of the surface coating on the separators concentrates on various functional polymers[12,13] or polar compounds[14,15]. For instance, Chen *et al.* developed a Fe,N co-doped mesoporous carbon sphere (Fe-N-MCS) as a coating material of polypropylene (PP) separators, which not only created a physical block to restrain LiPSs but also contributed to abundant adsorption sites for LiPS conversion[16]. Yu *et al.* prepared hexagonal MnO nanoflakes with rich oxygen vacancies incorporated with N-doped carbon nanotubes (NCNTs) to modify the separator. The NCNTs served as a physical barrier and conductive matrix, and MnO provided chemical adsorption and catalytic capability towards LiPSs[17]. Most of these candidates can physically/chemically interact with LiPSs while accelerating their redox reaction; however, they always exhibited insufficient shuttle restriction and catalytic activity, particularly when the sulfur loading on the cathode is high. Based on the above consideration, achieving the synergetic effect of completely suppressing the "shuttle effect" and effectively catalyzing LiPS conversion still remains challenging.

Zeolite molecular sieve is a kind of aluminosilicate with very regular nanoscale pore sizes between 0.3 and 1 nm[18,19], high surface area, conspicuous mechanical strength, and superior thermal stability[20,21]. The zeolite with unique internal channels is promising to totally block LiPSs on the cathode side without affecting the Li^+ transport as a functionalized coating on the separator, consequently adequately restraining the "shuttle effect". Meanwhile, polar metal sulfides (e.g., ZnS, CoS_3, and MoS_2)[22-24] have been extensively studied in Li-S batteries as excellent catalysts for sulfur reaction owing to their strong adsorption capability and catalytic activity. On the one hand, they are highly sulfurophilic, providing good chemical affinity/compatibility for the sulfur species. On the other hand, the sulfur atoms in metal sulfides possess high electronegativity, hence capturing electrons from the metals and offering active sites to stabilize the intermediates[25]. In addition, these sulfides generally exhibit better electrical conductivity than corresponding metal oxides, preferable for the redox reaction of sulfur species. Therefore, various metal sulfides can be employed on the separator to achieve strong adsorption and rapid conversion of the LiPSs[26] and eliminate the risk of accumulated LiPSs blocking the channels of the separator.

Herein, we propose a novel bilayer modification on the separator *via* a facile coating method, which mainly consists of a bottom zeolite layer and a top ZnS layer. Benefiting from the synergetic effect of block and catalysis provided by the bilayer modifier mentioned above [Figure 1A], the Li-S cell reaches a distinguished initial specific capacity of 1,364.22 mAh g^{-1} at 0.2 C, and an average capacity attenuation of only 0.052% per

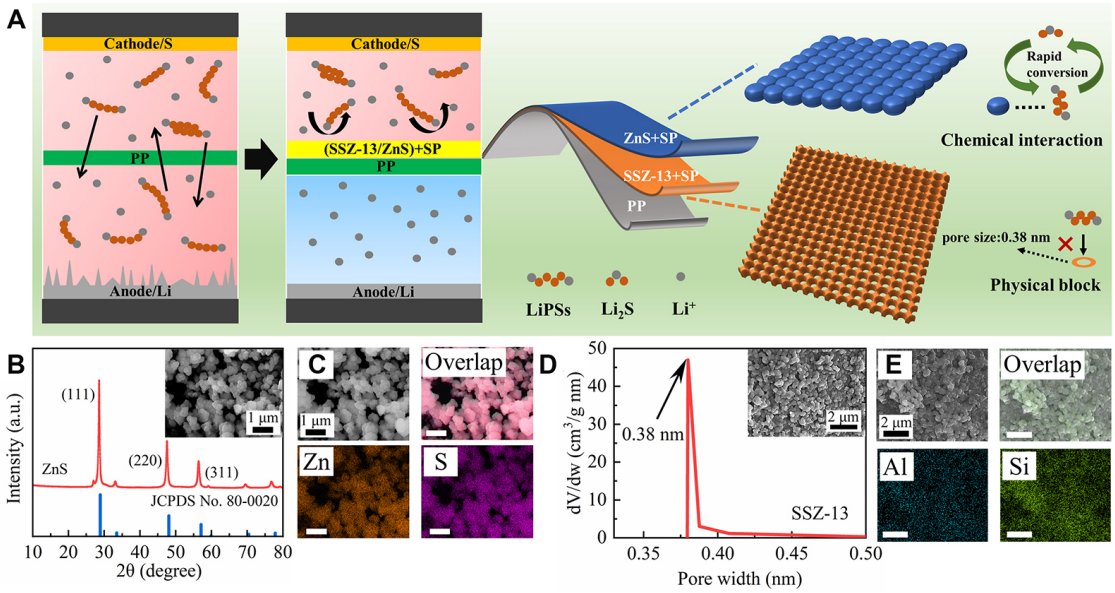

Figure 1. (A) Structure and function illustration of the SSZ-13/ZnS modified separator. (B) XRD pattern (inset is SEM image) and (C) corresponding elemental mappings of overlap, Zn and S. (D) Pore size distribution (inset is SEM image) and (E) corresponding elemental mappings of overlap, Al and Si.

cycle at 1 C upon 500 cycles, which is much superior to other cells with monolayer-modified and pristine separators. Even at a high sulfur loading and lean electrolyte condition, the cell with the bilayer coating separator maintains brilliant cycle stability. This work provides a fresh idea to design a synergistically modified separator used for constructing shuttle-free and highly stable Li-S batteries.

EXPERIMENTAL

Modified separator fabrications

The ZnS powder was synthesized using a simple hydrothermal method[27], where CH_4N_2S (99%, Innochem) and $Zn(Ac)_2{\cdot}2H_2O$ (99%, Innochem) were mixed uniformly in ethylene glycol with the molar ratio equal to 1:1 under continuous stirring. Then, the solution was transferred and sealed in a Teflon-lined stainless autoclave and heated at 180 °C for 24 h. Finally, the product was cleaned with distilled water and dried at 60 °C.

The zeolite molecular sieve (SSZ-13, Si/Al molar ratio of 25~30, Zhizhen), conductive carbon (Super P), and polyvinylidene fluoride (PVDF) were mixed in the N-Methyl-2-pyrrolidone (NMP) at a mass ratio of 8:1:1. The obtained SSZ-13 slurry was loaded on a piece of a commercialized PP separator (Celgard 2400) and then dried at 50 °C overnight to produce the SSZ-13@PP separator. The same method was used to prepare the ZnS slurry. The obtained ZnS slurry was coated on the pristine separator and SSZ-13@PP separator to further fabricate ZnS@PP- and SSZ-13/ZnS@PP-modified separators, respectively. The thickness of the coating layer can be regulated by the doctor blade gap and slurry viscosity. The final mass loading of the SSZ-13/ZnS coating on the separator was controlled at ~2.6 mg cm^{-2}.

Characterizations

The microcosmic morphologies of the materials and separators were observed by a Tescan Mira4 scanning electron microscope (SEM) equipped with an energy disperse spectrum (EDS) microanalyzer. The powder X-ray diffraction (XRD) measurement was performed on a Rigaku Ultima IV X-ray diffractometer with Cu-Kα radiation. The pore structure of the zeolite was measured on an ASAP 2460 analyzer by N_2

adsorption-desorption experiment. The ultraviolet-visible (UV-Vis) spectrum was recorded on a Shimadzu UV-3600 instrument. The X-ray photoelectron spectroscopy (XPS) was conducted on a Thermo Scientific K-Alpha instrument.

Electrochemical measurements

The sulfur cathode consisted of sulfur/mesoporous carbon (CMK-3, XF Nano) composite (prepared *via* melt-infiltration strategy at 155 °C for 12 h), Super P, and PVDF at a mass ratio of 8:1:1. The Li-S coin cell was assembled in an Ar-filled glove box, which was composed of a sulfur cathode and a lithium metal anode separated by a piece of pristine or modified separator. The coating layer in the modified separator was in contact with the sulfur cathode. The employed electrolyte was 1 M Lithium bis(trifluoromethanesulfonyl)imide (LiTFSI) and 2 wt% $LiNO_3$ dissolved in the mixed dimethyl ether/1,3-Dioxolane (DME/DOL) solvent (v/v = 1:1). The Li-S cell was cycled on a Neware tester in the voltage range of 1.7~2.8 V. The electrochemical workstation (PARSTAT MC) was used to measure cyclic voltammetry (CV) at different scan rates and electrochemical impedance spectra (EIS).

To investigate sulfur redox kinetics, a symmetrical cell with two identical electrodes was assembled in 0.05 M Li_2S_6/DME/DOL solution. The electrode was fabricated by mixing host material, Super P, and PVDF in the NMP at a weight ratio of 8:1:1, and then the obtained slurry was coated on the Al foil. CV measurement was performed at a scan rate of 10 mV s^{-1} in the voltage window of -0.8~0.8 V[22]. The galvanostatic intermittent titration technique (GITT) was conducted at 0.1 C for 15 min with the following rest for 2 h in the voltage range of 1.7~2.8 V. The Li-S cell was charged to 2.35 V at 0.2 C and then switched to a potentiostatic mode to monitor the shuttle current. The Li_2S deposition experiment was performed in a coin cell with 20 μL Li_2S_8 solution (0.2 M), employing carbon paper as the cathode and Li foil as the anode. The cell was first discharged to 2.06 V, and then the potential was kept at 2.05 V until the background current was below 10^{-5} A.

DFT computations

All theoretical calculations were conducted in a DMol3 module according to density functional theory (DFT). The exchange-correction function was described by the Perdew-Burke-Ernzerhof (PBE) within the generalized gradient approximation (GGA). The double numerical polarization (DNP) was selected as the basis setting. The all-electron relativistic method was adopted to manage the core and valence electrons. Grimme dispersion correction (DFT-D3) analyzed the van der Waals interaction. Linear/quadratic synchronous transit (LST/QST) methods identified the transition state and then determined the energy barrier of LiPS migration.

RESULTS AND DISCUSSION

The XRD pattern of as-prepared ZnS was provided in Figure 1B. Three characteristic peaks located at 28.9°, 48.1°, and 57.1° correspond to (111), (220), and (311) lattice planes of ZnS (JCPDS No. 80-0020), respectively, indicating successful preparation of the material. The inserted SEM image reveals a clear sphere morphology with the diameter distribution concentrated in the range of 50~100 nm [Supplementary Figure 1], matching the crystalline size calculated by the Debye-Scherrer equation[28] based on the XRD result. The EDS elemental mappings in Figure 1C demonstrate the uniform distribution of S and Zn elements in the spherical particles. These are all in line with expectations. For quantitative analysis of pores structure of commercialized SSZ-13, the N_2 absorption-desorption measurement was carried out. Figure 1D shows that pore sizes of the SSZ-13 are mainly centered around 0.38 nm. Additionally, the embedded SEM image reveals that SSZ-13 comprises uniform spherical units with diameters ranging from 0.27 to 0.45 μm. The EDS mapping in Figure 1E displays homogeneous distribution of Al and Si elements in the SSZ-13.

The above raw materials were coated on the pristine PP separator to create functionalized surface modification. Figure 2A shows the SEM image of the pristine PP separator, in which the micron-sized pores can be observed. These pores provide convenient channels for the electrolyte penetration and Li^+ movement. Nevertheless, they also allow LiPSs to pass through freely, leading to metal corrosion once they get in touch with the lithium anode. In contrast, Figure 2B and C provides the top and cross-sectional images of SSZ-13/ZnS@PP separators, respectively. It is observed that the pristine separator is uniformly covered by the SSZ-13 and ZnS particles with tiny pores, fabricating a continuous and flat coating layer with a total thickness of approximately 9 μm. Moreover, the EDS elemental mappings in Figure 2D distinctly exhibit that the elements of SSZ-13 (Al, Si) and ZnS (Zn, S) are separated into two layers, revealing a compact bilayer architecture on the pristine separator (The strong Al signal at the bottom is mainly attributed to the aluminum object platform). It needs to be emphasized that the monolayer-modified SSZ-13@PP and ZnS@PP separators are also dense and uniform without noticeable cracks, as shown in Supplementary Figure 2A and B in Supplementary Material.

The excellent mechanical property of the SSZ-13/ZnS@PP separator can be confirmed in Figure 2E since it remains intact after being folded several times, indicating ideal integration of the bilayer coating with the pristine separator substrate. In addition, the contact angle test evaluated the wettability of liquid electrolyte toward the modified separator. As depicted in Figure 2F, the SSZ-13/ZnS@PP separator offers a lower contact angle of 12° in contrast to the pristine separator (26°). It is considered that the polar ZnS particles on the top layer facilitate the rapid electrolyte penetration and, hence, Li^+ transport.

To explore the barrier capability of the SSZ-13/ZnS@PP separator, an H-shaped glass device was applied to compare the permeability of LiPSs across the separator. As shown in Figure 3A, 5 mL Li_2S_6 (25 mM) solution (left side) and 5 mL DOL/DME mixed solvent (right side) were separated by different separators. For the device composed of PP separators, the right solution color becomes yellow after 12 h and turns brown at last, indicating a free Li_2S_6 permeation. For the ZnS@PP case, the permeation did not stop, but the diffusion concentration decreases owing to the chemisorption of LiPSs on the surface of ZnS. When SSZ-13@PP and SSZ-13/ZnS@PP separators were employed, the solutions in the right chamber of the H-shaped device all remain colorless after 24 h, indicating the exceptional physical blocking capability of SSZ-13 towards LiPSs.

DFT calculation was implemented to investigate the three-dimensional structures of various LiPSs. As provided in Figure 3B, the sizes of several LiPS molecules are all well in excess of the pore size of SSZ-13 (3.8 Å) in any orientation (except the thickness of Li_2S_4/Li_2S_6) so that LiPS diffusion can be blocked completely by the zeolite. At the same time, the calculated diameter of Li^+ is about 0.076 nm so that the porosity of SSZ-13 satisfies the requests of transporting Li^+. Also, Li^+ prefers to be solvated by DME over DOL in the electrolyte, since the binding energies of Li^+-DME and Li^+-DOL ranged from 2.84 to 2.65 eV and from 1.71 to 1.69 eV, respectively[29,30]. The calculated diameter of $Li^+(DME)_1$ is 3.4 Å[31], smaller than the pore size of SSZ-13, implying the feasibility of Li^+ passing through the SSZ-13 pores without desolvation. To affirm it, the bulk resistance extracted from the Nyquist plot of a symmetrical stainless-steel cell calculated ionic conductivity of various separators according to the inserted equation in Figure 3C. It can be seen that the ionic conductivity of SSZ-13/ZnS-modified separators (1.14 mS cm^{-1}) is higher than that of the pristine one, attributed to facilitated Li^+ transport pathway provided by the porous SSZ-13 with suitable pore size and enhanced electrolyte wettability contributed by the polar ZnS. As a solution, the dense SSZ-13 zeolite, fabricated to adhere to the commercial separator, plays a critical role in sieving LiPSs and Li^+.

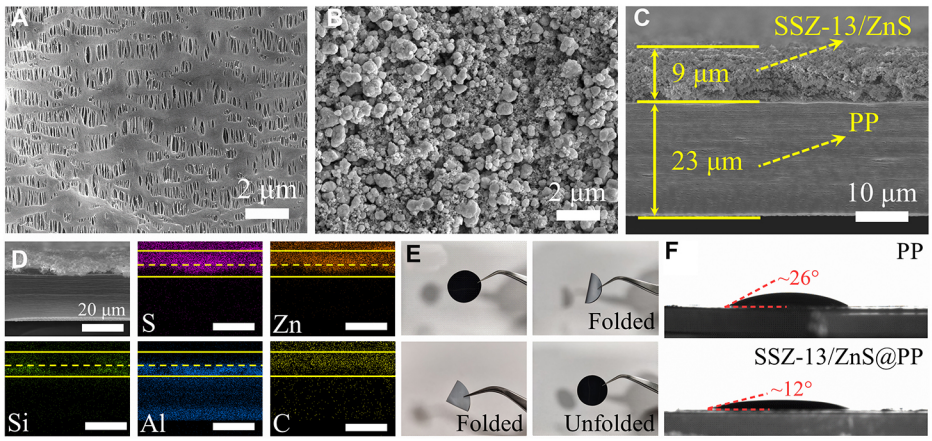

Figure 2. SEM images of (A) PP separator and (B) SSZ-13/ZnS@PP separator. (C) Cross-sectional image and (D) EDS elemental mappings of the SSZ-13/ZnS@PP separator. (E) Flexibility and (F) contact angle measurements of the SSZ-13/ZnS@PP separator.

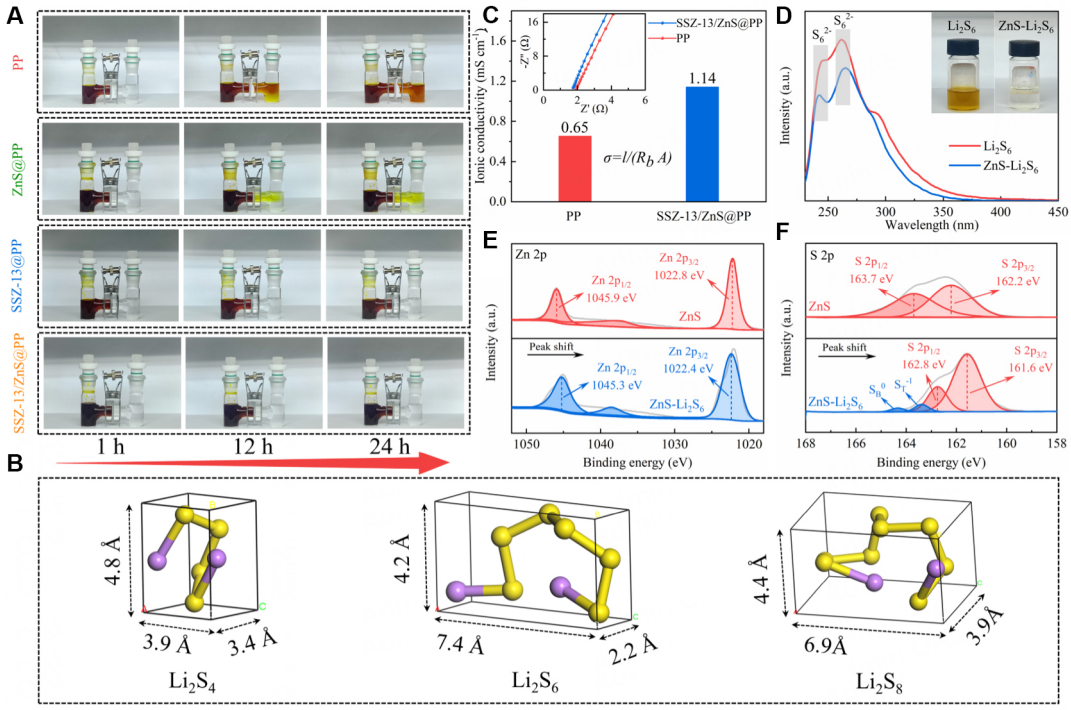

Figure 3. (A) LiPS diffusion tests in the H-shaped cells with different separators. (B) Molecular structures and calculated sizes of various LiPSs monomer units. (C) The calculated ionic conductivity for different separators. (D) UV-Vis spectra of Li_2S_6 solution before and after being adsorbed by the ZnS. (E) Zn 2p, (F) S 2p XPS spectra of ZnS before and after Li_2S_6 adsorption.

The chemical affinity of ZnS to LiPSs can be confirmed in the UV-Vis spectrum in Figure 3D, where the intensity of S_6^{2-} peak decreases prominently and the solution color becomes lighter after the ZnS powder was added into the LiPS solution. The latent interaction between LiPSs and ZnS was further investigated *via* XPS analyses. As shown in the Zn 2p spectra in Figure 3E, both Zn $2p_{3/2}$ and Zn $2p_{1/2}$ peaks shift towards lower binding energies after the ZnS was soaked in Li_2S_6 solution, suggesting the increased electron density at the metal center due to the polarization of electrons away from the terminal sulfur atoms (S_T^{-1}) in the Li_2S_6 to the electropositive Zn[32]. In the S 2p spectra [Figure 3F], two characteristic peaks located at 162.2 and 163.7 eV

ascribed to S^{2-} in the ZnS[32] show negative shifts after capturing Li_2S_6; meanwhile, the additional peaks relating to bridge sulfur (S_B^0) and S_T^{-1} in Li_2S_6[26] deliver positive shifts in the ZnS-Li_2S_6 compared to the pristine Li_2S_6 reported previously[33]. These confirm the strong interaction between ZnS and Li_2S_6 by forming chemical bonds. Overall, the above results clearly indicate that the SSZ-13 and ZnS play distinctive roles of physical barrier and chemical interaction on LiPSs, respectively, which guarantees the synergetic function of the modified separator.

The redox kinetic behaviors of the restrained LiPSs by the functionalized modification on the separator were investigated *via* various CV measurements. The CV curves of the symmetrical cell in Figure 4A show that the cell employing a ZnS electrode has higher current response than the SP electrode, revealing the latent catalytic activity of ZnS for accelerating the redox kinetics of those adsorbed LiPSs. The CV curves of the Li-S cells with modified and pristine separators at various scan rates are provided in Figure 4B and C, respectively. The observed shifts of cathodic and anodic peaks (O_a, R_a and R_b)[34] stand for the increased polarization at high scan rates. The lithium-ion diffusion coefficient (D_{Li^+}) as a key parameter for redox kinetics was calculated by the Randles-Sevcik equation below[35,36]:

$$I_p = (2.69\times10^5)n^{1.5}AD_{Li^+}^{0.5}C_{Li^+}v^{0.5}$$

Where I_p, n, A, C_{Li^+}, and v represent the peak current, electron transfer number in the reaction (n = 2), electrode area (1.54 cm^2), Li^+ concentration, and scan rate, respectively. So, the slopes of the curves (I_p-$v^{0.5}$) are positively correlated with the D_{Li^+}. As shown in Figure 4D-F and Supplementary Figure 3, the slope values and corresponding D_{Li^+} representing the SSZ-13/ZnS@PP separator are higher than the counterparts in each conversion step, demonstrating faster Li^+ diffusion rate and better sulfur redox kinetics in the entire charge/discharge processes.

The CV curves of Li-S cells using different separators at a scan rate of 0.1 mV s^{-1} are displayed in Figure 4G. Remarkably, the reduction peaks for SSZ-13/ZnS@PP separators exhibit a positive shift with significantly higher peak currents relative to other counterparts, verifying that the bilayer modification is conducive to the reversible conversion and then adequately utilizing sulfur species. The Tafel slope is calculated from the oxidation peak at ~2.39 V and reduction peak at ~2.03 V. The cell with the SSZ-13/ZnS@PP separator shows a lower Tafel slope value of 56 mV dec^{-1} for the oxidation from Li_2S to Li_2S_x [Figure 4H] and 38 mV dec^{-1} for the reduction from Li_2S_x to Li_2S [Figure 4I], compared to the PP case, suggesting the accelerated redox kinetics owing to the bidirectional catalysis capability of the synergetic structured coating[37].

To further confirm the catalytic effect of the SSZ-13/ZnS coating, the discharge products of sulfur cathodes matched with different separators were examined by XPS (the cells were discharged designedly to the low-potential plateau). As observed in Figure 5A, the characteristic peaks of S $2p_{3/2}$ at ~162.1 eV in the S 2p spectra are assigned to the generated Li_2S_2 during discharging[38]. The stronger Li_2S_2 signal on the cathode surface matched with the modified separator compared to the pristine one illustrates the accelerated sulfur reduction process. Besides, the Li_2S deposition experiment results are provided in Figure 5B and C for monitoring the formation of the discharge products. It can be seen that the accumulative capacity of deposited Li_2S in the modified separator far exceeds that of the PP separator (165.93 *vs.* 105.14 mAh g^{-1}), accompanied by higher current density and earlier precipitation time. This reveals that the SSZ-13/ZnS coating reduces the initial overpotential for the Li_2S nucleation and realizes faster growth of Li_2S[39].

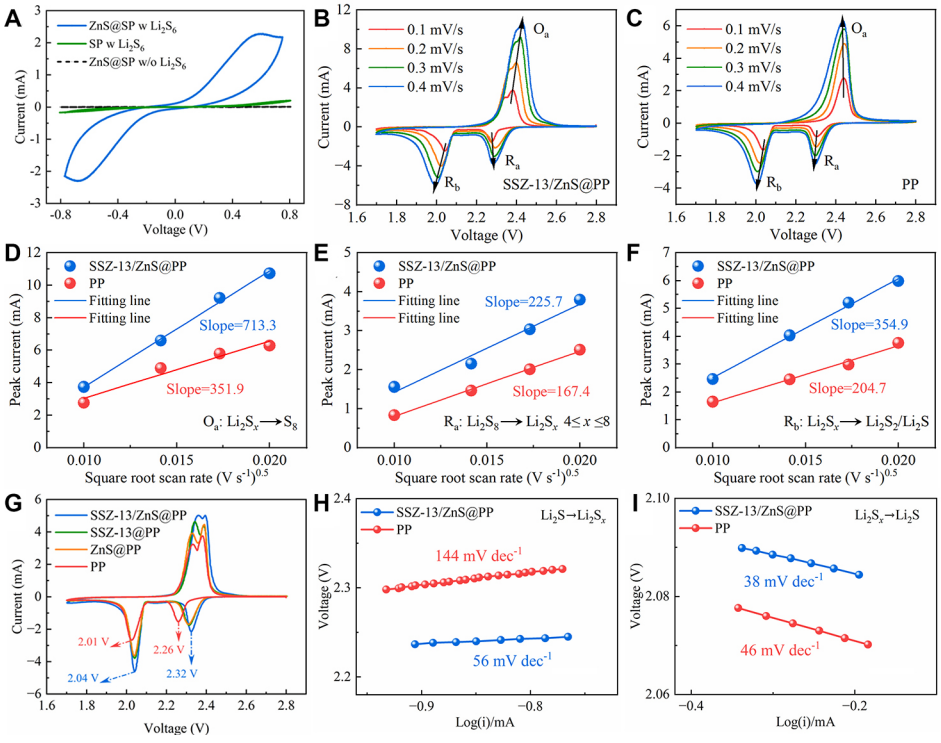

Figure 4. (A) CV curves of the symmetrical cells using different electrodes. CV curves of Li-S cells with (B) SSZ-13/ZnS@PP and (C) PP separator at various scan rates. Linear relationship of I_p-$v^{0.5}$ for (D) peak O_a, (E) peak R_a and (F) peak R_b. (G) CV curves of Li-S cells with various separators. Tafel slopes derived from the (H) oxidation peak and (I) reduction peak.

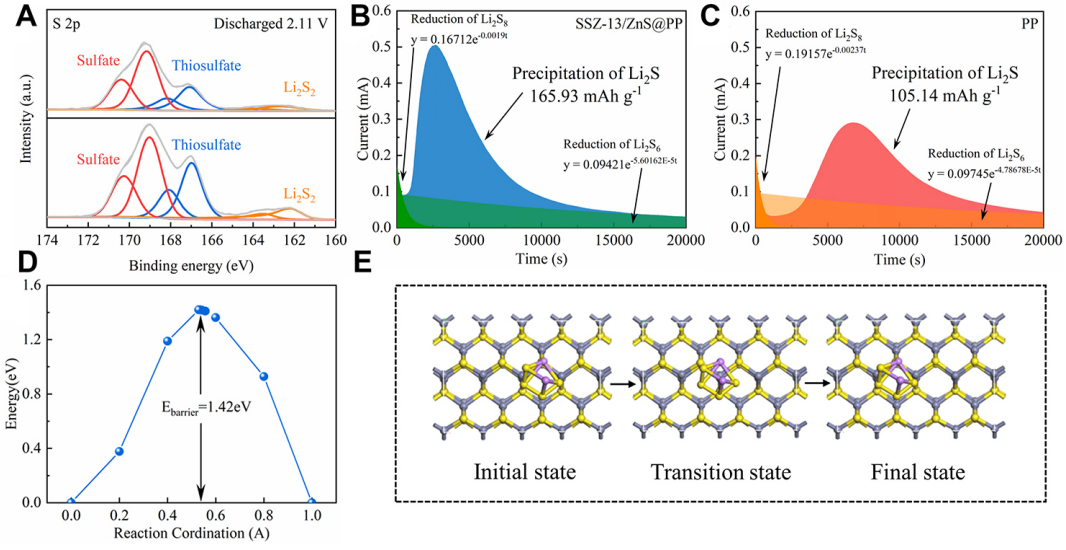

Figure 5. (A) S 2p XPS spectra of sulfur cathodes matched with different separators after discharging to 2.11 V. Potentiostatic discharge profiles of Li_2S deposition with (B) SSZ-13/ZnS@PP separator and (C) PP separator. (D) Energy profile for Li_2S_4 migration along the different adsorption sites on the ZnS (220) facet. (E) Li_2S_4 migration path on the ZnS (220) facet.

The LiPS migration usually depends on the exposed facets of the catalyst due to high surface affinity and reactivity. It was reported that the lowest energy shape of zinc blende nanoparticles is a rhombic dodecahedron, enclosed entirely by stoichiometric (220) facets[40]. Therefore, the geometrical configurations

of the minimum energy path for LiPS migration on the (220) facet of ZnS were investigated by DFT calculation (Li_2S_4 as the prototype for modeling). As provided in Figure 5D and E, the migration barrier for Li_2S_4 on the ZnS surface was only 1.42 eV. This benefits the rapid diffusion of Li_2S_4 to the nearby conductive area (e.g., SP particles in the coating)[41] and then electrochemical conversion.

Thus far, the above results well support the conclusion that the favorable entrapping-diffusion-conversion process of LiPSs can be realized by the separator modification strategy. It needs to be emphasized that the original concept of the SSZ-13/ZnS bilayer coating is chemically anchoring LiPSs and accelerating their conversion earlier to the physical block. In other words, the zeolite layer was set as a final defense for resisting LiPS diffusion. Mixing the zeolite and ZnS together in a monolayer can simplify the coating procedure. However, the block and catalytic capability towards LiPSs could be simultaneously weakened due to the incomplete coating of the SSZ-13 and ZnS on the separator. Thus, the bilayer design is essential for better exerting their synergetic effects.

The GITT test explored the effect of the functional coating on the conversion reaction process of the Li-S system. As shown in Figure 6A and B, compared to the PP sample, the cell with the SSZ-13/ZnS@PP separator displays smaller IR drops of QOCV (quasi-open-circuit voltage, 25.9 mV) and CCV (close-circuit voltage, 32.9 mV), suggesting the enhanced redox kinetics[42,43]. At the same time, the S_8 dissolution process of the SSZ-13/ZnS@PP and PP cells accounts for approximately 34% (8.93/25.9 h) and 37% (6.73/18.2 h) of the discharge phase, respectively. The relatively smaller proportion in the modified separator can be attributed to higher efficiency for Li_2S nucleation[44,45].

The Li-S full cell was assembled to investigate the actual contribution of the various modified coatings on the electrochemical performance. The discharge curves of these cells all deliver two well-defined potential plateaus, as exhibited in Figure 6C. However, larger capacity at low-potential plateau (Q_L) and higher Q_L/Q_H value in the SSZ-13/ZnS@PP cell manifest favorable conversion of LiPSs to insoluble sulfides[46,47]. A smaller polarization can also be observed with the SSZ-13/ZnS@PP separator, indicating enhanced electrochemical reversibility. The SSZ-13/ZnS@PP cell produces a high initial specific capacity (1,364.22 mAh g^{-1}) at 0.2 C; for comparison, the initial capacities of SSZ-13@PP, ZnS@PP, and pristine cells decrease to 1,085.25, 999.07, and 844.59 mAh g^{-1}, respectively. Furthermore, the highest reversible capacity of 992.28 mAh g^{-1} can be maintained in the SSZ-13/ZnS@PP cell after 140 cycles [Figure 6D], accompanied by a stable charge/discharge plateau during cycling [Supplementary Figure 4]. The shuttle current of the cell with the SSZ-13/ZnS@PP separator shown in Figure 6E is about 0.38 mA, apparently lower than that of a PP separator (≈0.60 mA). This proves the synergetic block and catalysis effect on LiPSs brought by the bilayer SSZ-13/ZnS modification, effectively restraining the "shuttle effect" and, hence, improving the cell performance. The powerful restriction on the redox shuttle further contributes to the homogeneous Li deposition and prevents the dendrite growth. It can be noticed in Supplementary Figure 5A that the cycled Li with a PP separator becomes rough with lots of cracks and particles. On the contrary, the Li surface with an SSZ-13/ZnS@PP separator after cycling [Supplementary Figure 5B] is apparently smooth without visible bulk aggregations.

The rate tests of Li-S cells with different separators were conducted at current densities ranging from 0.1 C to 2 C. The initial specific capacity with the SSZ-13/ZnS@PP separator reaches 1,383.47 mAh g^{-1} at 0.1 C (~82.7 % of the theoretical limit) and still sustains 904.36 mAh g^{-1} when the current density was raised to 2 C, all far beyond those with pristine and monolayer-coated separators [Figure 6F]. Additionally, the increased polarization at high rates is negligible [Supplementary Figure 6] and the recoverability of the cell capacity is proven after the discharge current back to 0.2 C. EIS measurement of Li-S cells was used to

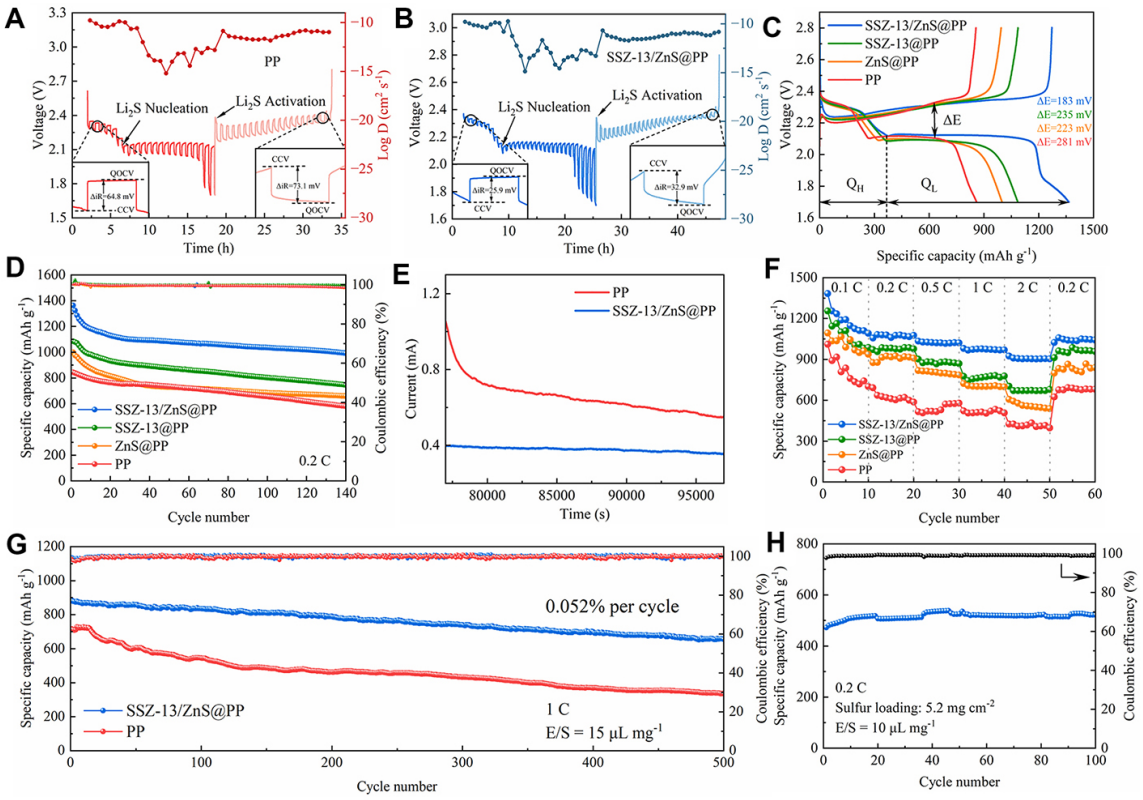

Figure 6. GITT measurements of the Li-S cells with (A) PP separator and (B) SSZ-13/ZnS@PP separator. (C) Comparison of charge/discharge profiles for different separators at 0.2 C. (D) Cycle stability of the Li-S cells with various separators at 0.2 C. (E) Shuttle currents of the Li-S cells with different separators. (F) Rate capabilities of the Li-S cells. (G) Long-term cycling performance of the Li-S cells at 1 C. (H) Cycle performance of the Li-S cell with SSZ-13/ZnS@PP separator at high sulfur loading at 0.2 C.

evaluate the difference in charge transfer process at open circuit voltage, where the semicircle in the high-frequency region stands for the charge transfer resistance (R_{ct}). As exhibited in Supplementary Figure 7, the SSZ-13/ZnS@PP cell delivers a lower R_{ct} value (48.0 Ω) compared with the PP (107.9 Ω), SSZ-13@PP (76.6 Ω), and ZnS@PP (82.8 Ω) cells, indicating an enhanced charge transfer kinetics brought by the bilayer modification on the separator. This merit and high ionic conductivity of the modified separator together contribute to the outstanding rate capability of the cell.

Besides, the long-term cycle stabilities of the Li-S cells at 1 C are exhibited in Figure 6G. The SSZ-13/ZnS@PP cell delivers a discharge capacity of 885.4 mAh g^{-1} and maintains at 655 mAh g^{-1} after 500 cycles with an attenuation rate of only 0.052% per cycle. The acquired cell performances with the separator modification strategy in this work are competitive and even superior to some recent reports adopting other coating materials (as summarized in Supplementary Table 1). Subsequently, the acceptable cycling capability of the Li-S cell with an SSZ-13/ZnS@PP separator at a higher sulfur loading of ~5.2 mg cm^{-2} and a lower E/S ratio of 10 uL mg^{-1} is also indicated in Figure 6H, reflecting great potential of the SSZ-13/ZnS@PP separator for practical applications.

CONCLUSIONS

In summary, we have successfully engineered a bilayer modification on the separator for Li-S cells, establishing an excellent synergetic relationship between inhibiting the diffusion of LiPSs and catalyzing their conversion. The experimental studies and DFT calculations reveal that the appropriate pore size of

SSZ-13 zeolite physically blocks the movement of the LiPSs towards the lithium anode but ensures free and rapid transport of Li^+. Additionally, the introduced ZnS coating chemically interacts and then accelerates the redox kinetics of the confined sulfur species by providing a low surface migration barrier. Consequently, the SSZ-13/ZnS@PP separator endows the Li-S cell with a high discharge capacity of 1,364.22 mAh g^{-1} at 0.2 C, preferable capacity decay of 0.052% per cycle over 500 cycles at 1 C, and satisfactory rate capability. This work provides a simple but effective strategy of separator structure engineering to develop advanced Li-S batteries for commercial applications.

DECLARATIONS

Authors' contributions

Methodology, writing-review & editing, funding acquisition: Ma Y
Investigation, data curation, writing-original draft: Chang L
Formal analysis, supervision: Yi D
Investigation, validation: Liu M, Wang P
Visualization, resources: Luo S, Zhang Z
Conceptualization, project administration, funding acquisition: Yuan Y, Lu H

Availability of data and materials

Not applicable.

Financial support and sponsorship

This work is supported by the National Natural Science Foundation of China (No. 51704222), Postdoctoral Science Foundation of China (2023M742243), Key Project of Natural Science Basic Research Plan of Shaanxi Province (No. 2022JZ-25), and Special Research Program of Shaanxi Provincial Education Department (No. 22JC049).

Conflicts of interest

All authors declared that there are no conflicts of interest.

Ethical approval and consent to participate

Not applicable.

Consent for publication

Not applicable.

REFERENCES

1. Xiang Y, Li J, Lei J, et al. Advanced separators for lithium-ion and lithium-sulfur batteries: a review of recent progress. *ChemSusChem* 2016;9:3023-39. DOI
2. Hu X, Ma Y, Qian J, et al. Self-induced dual-layered solid electrolyte interphase with high toughness and high ionic conductivity for ultra-stable lithium metal batteries. *Adv Mater* 2024;36:e2303710. DOI
3. Yang X, Luo J, Sun X. Towards high-performance solid-state Li-S batteries: from fundamental understanding to engineering design. *Chem Soc Rev* 2020;49:2140-95. DOI PubMed
4. Ma F, Wan Y, Wang X, et al. Bifunctional atomically dispersed Mo-N_2/C nanosheets boost lithium sulfide deposition/decomposition for stable lithium-sulfur batteries. *ACS Nano* 2020;14:10115-26. DOI
5. Ma Y, Qu W, Hu X, et al. Induction/inhibition effect on lithium dendrite growth by a binary modification layer on a separator. *ACS Appl Mater Interfaces* 2022;14:44338-44. DOI
6. Fang R, Zhao S, Sun Z, Wang DW, Cheng HM, Li F. More reliable lithium-sulfur batteries: status, solutions and prospects. *Adv Mater*

2017;29:1606823. DOI
7. Xia S, Zhang X, Liang C, Yu Y, Liu W. Stabilized lithium metal anode by an efficient coating for high-performance Li-S batteries. *Energy Stor Mater* 2020;24:329-35. DOI
8. Liu X, Wang J, Zhu F, et al. Surface oxygen vacancy engineering in weak Bi-O bonded ferroelectric bismuth sodium titanate for boosting the photocatalytic CO_2 reduction reaction. *J Mater Chem A* 2024;12:9661-71. DOI
9. Jiang FN, Yang SJ, Cheng XB, et al. Thermal safety of dendritic lithium against non-aqueous electrolyte in pouch-type lithium metal batteries. *J Energy Chem* 2022;72:158-65. DOI
10. Tan K, Liu Y, Tan Z, Zhang J, Hou L, Yuan C. High-yield and *in situ* fabrication of high-content nitrogen-doped graphene nanoribbons@Co/CoOOH as an integrated sulfur host towards Li-S batteries. *J Mater Chem A* 2020;8:3048-59. DOI
11. Deng N, Kang W, Liu Y, et al. A review on separators for lithium sulfur battery: progress and prospects. *J Power Sources* 2016;331:132-55. DOI
12. Gao S, Wang K, Wang R, et al. Poly(vinylidene fluoride)-based hybrid gel polymer electrolytes for additive-free lithium sulfur batteries. *J Mater Chem A* 2017;5:17889-95. DOI
13. Jin Z, Xie K, Hong X, Hu Z, Liu X. Application of lithiated Nafion ionomer film as functional separator for lithium sulfur cells. *J Power Sources* 2012;218:163-7. DOI
14. Jiang K, Gao S, Wang R, et al. Lithium sulfonate/carboxylate-anchored polyvinyl alcohol separators for lithium sulfur batteries. *ACS Appl Mater Interfaces* 2018;10:18310-5. DOI
15. Zheng B, Li J, Wang L, et al. Hydrogen storage in MXenes: controlled adjustment of sorption by interlayer distance and transition metal elements. *Int J Hydrogen Energy* 2024;50:1555-61. DOI
16. Chen D, Zhu M, Zhan W, et al. Fe, N co-doped mesoporous carbon spheres as barrier layer absorbing and reutilizing polysulfides for high-performance Li-S batteries. *J Mater Sci* 2022;57:13527-40. DOI
17. Yu X, Chen W, Cai J, Lu X, Sun Z. Oxygen vacancy-rich MnO nanoflakes/N-doped carbon nanotubes modified separator enabling chemisorption and catalytic conversion of polysulfides for Li-S batteries. *J Colloid Interface Sci* 2022;610:407-17. DOI
18. Wang Z, Yu J, Xu R. Needs and trends in rational synthesis of zeolitic materials. *Chem Soc Rev* 2012;41:1729-41. DOI
19. te Hennepe HJC, Boswerger WBF, Bargeman D, Mulder MHV, Smolders CA. Zeolite-filled silicone rubber membranes experimental determination of concentration profiles. *J Membr Sci* 1994;89:185-96. DOI
20. Shekarian E, Jafari Nasr MR, Mohammadi T, Bakhtiari O, Javanbakht M. Preparation of 4A zeolite coated polypropylene membrane for lithium-ion batteries separator. *J Appl Polym Sci* 2019;136:47841. DOI
21. Yu L, Miao J, Jin Y, Lin JYS. A comparative study on polypropylene separators coated with different inorganic materials for lithium-ion batteries. *Front Chem Sci Eng* 2017;11:346-52. DOI
22. Lin H, Yang L, Jiang X, et al. Electrocatalysis of polysulfide conversion by sulfur-deficient MoS_2 nanoflakes for lithium-sulfur batteries. *Energy Environ Sci* 2017;10:1476-86. DOI
23. Peng H, Zhang Y, Chen Y, et al. Reducing polarization of lithium-sulfur batteries via ZnS/reduced graphene oxide accelerated lithium polysulfide conversion. *Mater Today Energy* 2020;18:100519. DOI
24. Yang X, Gao X, Sun Q, et al. Promoting the transformation of Li_2S_2 to Li_2S: significantly increasing utilization of active materials for high-sulfur-loading Li-S batteries. *Adv Mater* 2019;31:e1901220. DOI
25. Wu J, Ye T, Wang Y, et al. Understanding the catalytic kinetics of polysulfide redox reactions on transition metal compounds in Li-S batteries. *ACS Nano* 2022;16:15734-59. DOI
26. Xu J, Zhang W, Fan H, Cheng F, Su D, Wang G. Promoting lithium polysulfide/sulfide redox kinetics by the catalyzing of zinc sulfide for high performance lithium-sulfur battery. *Nano Energy* 2018;51:73-82. DOI
27. Su D, Kretschmer K, Wang G. Improved electrochemical performance of Na-ion batteries in ether-based electrolytes: a case study of ZnS nanospheres. *Adv Energy Mater* 2016;6:1501785. DOI
28. Sundararajan M, Sakthivel P, Fernandez AC. Structural, optical and electrical properties of ZnO-ZnS nanocomposites prepared by simple hydrothermal method. *J Alloys Compd* 2018;768:553-62. DOI
29. Tsuzuki S, Shinoda W, Seki S, et al. Intermolecular interactions in Li^+-glyme and Li^+-glyme-TFSA-complexes: relationship with physicochemical properties of [Li (glyme)][TFSA] ionic liquids. *Chemphyschem* 2013;14:1993-2001. DOI
30. Xie Z, Wu Z, An X, et al. 2-fluoropyridine: a novel electrolyte additive for lithium metal batteries with high areal capacity as well as high cycling stability. *Chem Eng J* 2020;393:124789. DOI
31. Jeon T, Jung SC. The molecular sieving mechanism of a polysulfide-blocking metal-organic framework separator for lithium-sulfur batteries. *J Mater Chem A* 2021;9:23929-40. DOI
32. Yang J, Zhao S, Lu Y, Zeng X, Lv W, Cao G. ZnS spheres wrapped by an ultrathin wrinkled carbon film as a multifunctional interlayer for long-life Li-S batteries. *J Mater Chem A* 2020;8:231-41. DOI
33. He J, Luo L, Chen Y, Manthiram A. Yolk-shelled C@Fe_3O_4 nanoboxes as efficient sulfur hosts for high-performance lithium-sulfur batteries. *Adv Mater* 2017;29:1702707. DOI
34. Zeng P, Liu C, Zhao X, et al. Enhanced catalytic conversion of polysulfides using bimetallic Co_7Fe_3 for high-performance lithium-sulfur batteries. *ACS Nano* 2020;14:11558-69. DOI
35. Tao X, Wang J, Liu C, et al. Balancing surface adsorption and diffusion of lithium-polysulfides on nonconductive oxides for lithium-sulfur battery design. *Nat Commun* 2016;7:11203. DOI PubMed PMC
36. Rui X, Ding N, Liu J, Li C, Chen C. Analysis of the chemical diffusion coefficient of lithium ions in $Li_3V_2(PO_4)_3$ cathode material.

Electrochim Acta 2010;55:2384-90. DOI

37. Wang X, Han J, Luo C, et al. Coordinated adsorption and catalytic conversion of polysulfides enabled by perovskite bimetallic hydroxide nanocages for lithium-sulfur batteries. *Small* 2021;17:e2101538. DOI
38. Lu H, Liu M, Zhang X, et al. Catalytic effect of ammonium thiosulfate as a bifunctional electrolyte additive for regulating redox kinetics in lithium-sulfur batteries by altering the reaction pathway. *ACS Appl Mater Interfaces* 2024;16:13640-50. DOI
39. Wang M, Fan L, Sun X, et al. Nitrogen-doped $CoSe_2$ as a bifunctional catalyst for high areal capacity and lean electrolyte of Li-S battery. *ACS Energy Lett* 2020;5:3041-50. DOI
40. Barnard AS, Feigl CA, Russo SP. Morphological and phase stability of zinc blende, amorphous and mixed core-shell ZnS nanoparticles. *Nanoscale* 2010;2:2294-301. DOI PubMed
41. Zhou T, Lv W, Li J, et al. Twinborn TiO_2-TiN heterostructures enabling smooth trapping-diffusion-conversion of polysulfides towards ultralong life lithium-sulfur batteries. *Energy Environ Sci* 2017;10:1694-703. DOI
42. Lei D, Shang W, Zhang X, et al. Facile synthesis of heterostructured MoS_2-MoO_3 nanosheets with active electrocatalytic sites for high-performance lithium-sulfur batteries. *ACS Nano* 2021;15:20478-88. DOI
43. Li C, Qi S, Zhu L, et al. Regulating polysulfide intermediates by ultrathin Co-Bi nanosheet electrocatalyst in lithium-sulfur batteries. *Nano Today* 2021;40:101246. DOI
44. Park J, Kim ET, Kim C, et al. The importance of confined sulfur nanodomains and adjoining electron conductive pathways in subreaction regimes of Li-S batteries. *Adv Energy Mater* 2017;7:1700074. DOI
45. Wang B, Wang L, Zhang B, et al. Niobium diboride nanoparticles accelerating polysulfide conversion and directing Li_2S nucleation enabled high areal capacity lithium-sulfur batteries. *ACS Nano* 2022;16:4947-60. DOI
46. Qin B, Cai Y, Wang P, Zou Y, Cao J, Qi J. Crystalline molybdenum carbide-amorphous molybdenum oxide heterostructures: in situ surface reconfiguration and electronic states modulation for Li-S batteries. *Energy Stor Mater* 2022;47:345-53. DOI
47. Zeng Q, Li X, Gong W, et al. Copolymerization of sulfur chains with vinyl functionalized metal-organic framework for accelerating redox kinetics in lithium-sulfur batteries. *Adv Energy Mater* 2022;12:2104074. DOI